



A new Metallic Thermal Barrier Coating System for Rocket Engines: Failure Mechanisms and Design Guidelines

T. Fiedler¹ · J. Rösler¹ · M. Bäker¹

Submitted: 3 May 2019 / in revised form: 23 July 2019 / Published online: 5 August 2019
© ASM International 2019

Abstract To protect liquid rocket combustion chamber walls, a coating may be applied on the hot gas side. Recently, a new metallic coating system, applied with high-velocity oxyfuel spray, has been developed. To investigate the damage mechanisms of these coatings under large thermal loads, laser cycling experiments were performed, where the coating surface is heated up with a high-power laser to get a large temperature gradient, similar to the conditions in the combustion chamber. In these laser cycling tests, different damage mechanisms like large-scale buckling of the coatings or vertical cracks were observed. The main aim of this paper is to understand the failure mechanisms and to identify critical loads leading to coating failure. Tensile tests, laser cycling experiments and finite element simulations were carried out to determine critical elastic strains for crack initiation and gain a better understanding of the mechanisms and the critical loads for buckling.

Keywords aerospace · MCrAlY · HVOF · thermal cycling · interface cracking · finite element modeling

Introduction

Combustion chambers of large liquid-fuel rocket engines like the Vulcain 2 are exposed to large thermal loads. Although the combustion chamber is regeneratively cooled by cryogenic fuel in internal cooling channels

(Ref 1, 2), damage mechanisms like blanching (Ref 3, 4) and the doghouse effect (Ref 5-9) can be observed. These failure mechanisms are a limiting factor on the combustion chamber life. To increase the combustion chamber lifetime with respect to reusability and to enhance the efficiency by increasing the hot gas temperatures and pressures, the combustion chamber wall may be protected by a thermal barrier coating. This coating reduces the maximum temperature of the combustion chamber wall material and protects the wall against the oxidizing atmosphere.

In preliminary work (Ref 10-13), a new coating system was developed based on the findings from previous studies (see “[Development of a New Coating System](#)” section). In the present study, this coating system is tested in laser cycling experiments with a high heat flux to provoke different damage mechanisms like vertical cracks or interface separations. These damage mechanisms are elucidated in detail, assisted by finite element simulations. Critical loads for interfacial failure and for the growth of vertical cracks were determined from the simulations. Tensile tests on coated samples were used to validate the critical strains for vertical crack growth.

Based on the investigations in the present work, design guidelines are provided for coating design in rocket combustion chambers. The critical loads for coating failure can be transferred to a failure model for coating design and coating lifetime prediction in the combustion chamber.

Thermal Barrier Coatings for Rocket Combustion Chambers

Thermal barrier coatings (TBC) are state of the art in stationary gas turbines and aero engines (Ref 14, 15). Usually, they consist of a metallic bondcoat and a ceramic topcoat

✉ T. Fiedler
t.fiedler@tu-braunschweig.de

¹ Institute for Materials, Technische Universität Braunschweig, Langer Kamp 8, 38106 Brunswick, Germany

(Ref 16–18). But the harsh environmental loads in rocket combustion chambers necessitate the development of new coating concepts.

For rocket combustion chambers, coatings with ceramic topcoats as used in gas turbines and aero engines were, for example, tested by NASA (Ref 8, 19), within the German National Technology Programme on Cryogenic Rocket Engines TEKAN (Ref 20–22), at the German Aerospace Centre (Ref 5, 23, 24), at the Keldysh Research Centre Moscow (Ref 25) and within the current German research project SFB TRR40 (Ref 13, 26–28).

In thermal tests, some of these ceramic coatings showed a good performance and a significant increase in the combustion chamber lifetime (Ref 5, 8, 24). But in experiments with large heat fluxes and thus large temperature gradients, namely plasma-assisted burner rig (Ref 25) and laser cycling experiments (Ref 13, 26, 28), delamination, buckling and spalling of the coatings were observed. Furthermore, due to the large heat flux, very thin ceramic coatings are necessary (Ref 29), and the high heat flux combined with the low thermal conductivity will lead to extreme temperature gradients and thus thermo-mechanical loads in the ceramic coatings.

Other work focused on metallic coating systems: Different variations of NiCrAlY or NiAl were tested (Ref 30–32) as well as chromium topcoats (Ref 33, 34) or a mixture of chromium and copper (Ref 32, 35, 36) or chromium, copper and aluminum (Ref 37, 38). These coatings showed a good oxidation resistance and a sufficient protection of the combustion chamber wall (Ref 35, 37, 38). The coatings were mostly tested in isothermal oxidation tests or in burner rig tests with low heat fluxes (see also “[Laboratory-Scale Thermal Testing of TBC](#)” section), where no significant coating damage was observed (Ref 31, 32, 36). A full-scale engine test with a chromium topcoat in the Russian RD-180 engine led to the formation of vertical cracks propagating from the chromium surface into the nickel bondcoat, but the combustion chamber showed no damage, not even geometrical changes (Ref 33).

The different chemical compositions and coefficients of thermal expansion of the substrate material (copper and copper alloys, see “[Thermomechanical Loads on the Coatings](#)” section) and the coatings require a bondcoat. NiCrAlY bondcoats, as used in gas turbines and aero engines, are not suitable here: On the one hand, the mismatch in thermal expansion between copper alloy and NiCrAlY leads to microcracks at the interface and even a delamination of the coatings (Ref 13, 26, 39). On the other hand, the chemical gradient leads to interdiffusion and the formation of diffusion pores at the interface (Ref 32, 40). Consequently, other bondcoats were tested, for example a CuCrAl alloy (Ref 32). Other studies focused on graded coatings consisting of copper (or copper alloy) and the

topcoat material (Ref 41, 42). In the studies with CuCr topcoats, no bondcoat was necessary (Ref 32).

Development of a New Coating System

In preliminary studies (Ref 10–13), a new coating system has been developed based on the findings from previous research. The development focused on a metallic coating system since it was found that ceramic coatings were not suitable for the high heat fluxes in the combustion chamber (see above). Although, in standard TBC applications, a ceramic topcoat is essential for a sufficient thermal insulation, the large cooling heat flux in the rocket combustion chamber and the high thermal conductivity of the copper wall (larger by a factor of 15 than the thermal conductivity of the metallic coatings) lead to an adequate insulation by the metallic coatings.

To enhance the coating adhesion, a bondcoat was developed additionally. The coatings were applied with the high-velocity oxyfuel spray (HVOF) process. The main advantage of HVOF, compared to other atmospheric spray processes, is the high particle velocity. This results in a short time exposure of the particles in the oxidizing flame (oxide content in the coatings < 1%) and a large kinetic energy of the particles and thus a relatively good adhesion and a dense coating structure (porosity < 1%) (Ref 12, 43, 44).

For the topcoat, the nickel-based superalloy Rene80 (Ref 45) was chosen (Ref 10). It has the composition Ni-Cr14-Co9.5-Ti5-Mo4-W4-Al3 (wt.%), a high solidus temperature of 1493 K and a good high temperature strength and oxidation resistance (Ref 45, 46).

For the bondcoat, a new NiCuCrAl alloy was developed by modification of existing NiCrAlY alloys (Ref 11). It has the composition Ni-Cu30-Al6-Cr5 (wt.%). The addition of copper enhances the chemical compatibility and reduces the mismatch in thermal expansion between copper-based substrate and nickel-based coating (Ref 13). The better chemical compatibility results in a better interdiffusion and thus adhesion of the coatings (Ref 10). The mismatch in thermal expansion would have led to large thermal stresses at the rough interface between coating and substrate (Ref 12, 13) and thus the formation of delamination cracks. Since the newly developed alloy has an intermediate coefficient of thermal expansion between copper and the topcoat alloy (Ref 11), these stresses could be reduced (Ref 12).

Laboratory-Scale Thermal Testing of TBC

The short review in “[Thermal Barrier Coatings for Rocket Combustion Chambers](#)” section shows that it is essential to test the coatings under high heat loads to investigate

realistic damage mechanisms. A large heat flux is necessary to reproduce the thermal shock and the high temperature gradient in the combustion chamber wall and thus high thermal strains (see “[Thermomechanical Loads on the Coatings](#)” section).

TBCs for gas turbines are, for example, tested in burner rig tests, where the coating surface is heated by a hot-gas flow, while the substrate’s backside is cooled by pressurized air. In these tests, surface temperatures of 1773 K or more can be achieved within a few seconds, and the maximum heat flux can reach 0.1–1 MW/m² (Ref 16, 47). These loads are suitable to test coatings for turbine engine application; however, for rocket engines, larger heat fluxes are necessary.

Larger heat fluxes can be, for example, achieved with plasma jets: In a test bed at the Keldysh Research Centre in Moscow, heat fluxes of up to 26 MW/m² were achieved with plasma heating of the coating surface and high-pressure water cooling of the substrate (Ref 25). Another possibility to produce large heat fluxes is heating with laser radiation. The laser beam can be moved over the surface (Ref 48) or divergently widened with a special optics to produce a broad laser spot on the surface (Ref 49–54). With laser powers in the order of magnitude of some kilowatts, high heating rates can be achieved. This results on the one hand in a thermoshock. On the other hand, a large thermal gradient can be achieved even without cooling on the backside during the first seconds of the experiments (Ref 48, 51, 52). In experiments without a cooling system, heat fluxes of approximately 2 MW/m² are reached (Ref 51, 52). With cooling, for example with liquid nitrogen, heat fluxes of 8.5 MW/m² [measurement (Ref 50)] to 22.5 MW/m² [simulations (Ref 49)] are reported (these experiments were conducted without a coating).

In the framework of the present research project SFB TRR40, a miniature combustion chamber is currently under development, where coated test panels will be examined in the future. In the final configuration, the heat flux will reach a magnitude of 14 MW/m² and a combustion chamber a pressure of up to 40 bar (Ref 55).

The largest heat fluxes under which TBCs were tested so far were achieved in a full-scale engine test of the Russian RD-180 engine with 48.4 MW/m² (Ref 33, 34). But since these full-scale tests are extremely expensive, they can only be used for a final qualification of a coating system. For coating development, a laboratory-scale experiment should be used to be able to carry out a suitable number of experiments.

Within the coating development of the present project SFB TRR40, a thermal shock laser test bed has been built up which uses a 3.3 kW diode laser to heat the coating surface (Ref 26). Depending on the diameter of the laser spot, heat flux densities of up to 30 MW/m² are possible.

Although this laser experiment does not reproduce the very high heat flux in rocket combustion chambers (up to 150 MW/m², see “[Thermomechanical Loads on the Coatings](#)” section), it goes beyond many other laboratory-scale experiments.

The laser cycling experiment is used in the present study to provoke different damage mechanisms: Interface damage such as microcracks or pores was observed as well as large-scale buckling or vertical cracking of the coatings. A thermally grown oxide (TGO) at the interfaces, like in gas turbine coatings, was not observed here due to the relatively dense HVOF coatings and thus low oxygen permeability.

From the findings in the laser cycling experiment, critical loads for failure were analyzed which are elucidated in finite element simulations. The critical loads can then be transferred to simulations of rocket combustion chambers to predict possible in-service failure mechanisms and calculate the coatings’ lifetime.

Thermo-mechanical Loads on the Coatings

For coating design, it is essential to know the thermal and mechanical loads in the combustion chamber. Furthermore, the loads in the laboratory-scale experiments, in this case the laser cycling experiment, have to be investigated to qualify the coatings based on these experiments.

Rocket Combustion Chamber

The hot gas in cryogenic rocket engines like the space shuttle main engine or the Vulcain 2 engine reaches temperatures of up to 3500–3800 K (Ref 56, 57). Since no engineering material can withstand these high temperatures, the combustion chamber has to be cooled, which is normally done with cryogenic fuel (in this case hydrogen) in internal cooling channels in the chamber wall. To enable a good cooling heat flux, the chamber wall is made of a high thermal conductive copper alloy, mostly CuAgZr (Ref 3, 36, 49, 58). This copper liner with its cooling channels is surrounded by a stiff nickel jacket.

The cooling generates a wall heat flux of up to 150 MW/m² (Ref 42, 59, 60). This results in a large temperature difference between the hot copper liner and the cold nickel jacket and thus large thermal strain differences. Compared to the hot copper alloy, the cold nickel jacket is stiff and constrains the thermal expansion of the copper wall. Thus, large compressive strains are induced on the hot gas side. Neglecting the comparatively small strains in the nickel jacket, the compressive strains on the hot gas side are only dependent on the temperature and the coefficient of thermal expansion of the material. If a coating is applied to the hot-gas side of the copper liner, it is also exposed to large compressive strains.

With a coefficient of thermal expansion of $16 \times 10^{-6}/\text{K}$ (Rene80 topcoat (Ref 10)) and assuming a temperature increase of approximately 1000 K compared to the cooled nickel jacket, these strains reach a magnitude of 1.6%, in accordance with finite element simulations of a rocket combustion chamber (Ref 61). The elastic strains evolving during a combustion cycle determined in finite element simulations are plotted in Fig. 1: At the beginning of the cycle (after the pre-cooling in the case of the combustion chamber), the large heat flux leads to an increase in the surface temperature. The constraint by the cold nickel jacket leads to large elastic compressive strains ($\epsilon_{E11} < 0$). Due to yielding at high temperatures, the elastic strains are reduced with further heating. Subsequent cooling down leads to a contraction of the previously hot coating. Due to the large plastic deformation at high temperature, the cooling induces high elastic tensile strains in the coating of 0.1–0.2%. This cooling phase is not only important for reusable engines: Also single use engines exhibit this cooling phase after a test run prior to the flight. For a more detailed discussion, see Ref 10, 61.

The large elastic compressive strains during heating may lead to buckling and spalling of applied coatings. The tensile strains upon cooling may lead to the growth of vertical cracks, as seen in the Russian RD-180 engine with a chromium topcoat (Ref 33, 34) (see “Thermal Barrier Coatings for Rocket Combustion Chambers” section).

Laser Cycling Experiment for Thermal Shock Testing

In the laser cycling experiments, the surface of a coating, applied on a cylindrical copper block, is heated with a high-power laser (for details see “Thermal Cycling”

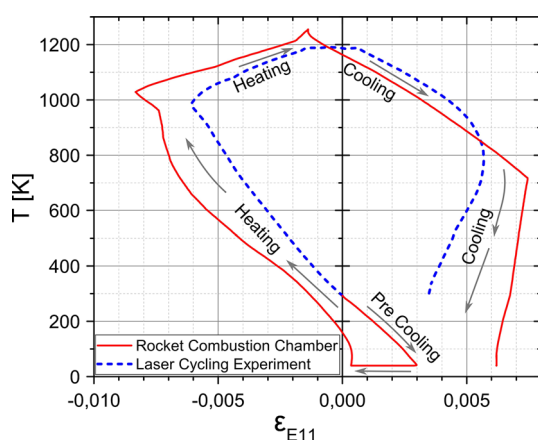


Fig. 1 Elastic strains from FEM simulations near the coating surface for a 90- μm -thick coating in a rocket combustion chamber (already published in Ref 10) and in the laser cycling experiment (simulations according to “FEM Model of the Laser Sample” section). The coating in the combustion chamber is additionally exposed to a pre-cooling of the engine

section). The fast heating rate of the high-power laser generates a thermal shock, and the capacitive cooling by the relatively high substrate volume (16 cm^3 in the present study) leads to a heat flux of up to 30 MW/m^2 through the coating within the first few seconds of the experiment. This high heat flux causes a large temperature gradient in the sample, even without an active cooling of the substrate. This results in mechanical loads similar to the loads in the combustion chamber (see “Rocket Combustion Chamber” section): Large compressive strains evolve during heating, and the coatings yield at high temperature. A subsequent cooling in cold water leads to tensile strains.

The elastic strains evolving during a laser cycle are plotted in Fig. 1 for comparison with the rocket cycle: At the beginning of the cycle (after the pre-cooling in case of the combustion chamber), the large heat flux leads to an increase in the surface temperature. The cold substrate in the laser experiment constrains the coating and leads to large elastic compressive strains ($\epsilon_{E11} < 0$). Due to yielding at high temperatures, the elastic strains are reduced with further heating. Subsequent cooling down leads to the formation of elastic tensile strains ($\epsilon_{E11} > 0$). For a more detailed discussion, see Ref 10, 61. The comparison between laser experiment and rocket cycle shows that there are still differences in the mechanical loads in the coatings, but the laser experiment leads to qualitatively similar loading conditions.

Methods

Coating Process

The coatings in this work were applied with the high-velocity oxyfuel spray (HVOF) process. Rene80 (Ni-Cr14-Co9.5-Ti5-Mo4-W4-Al3) for topcoat and NiCuCrAl (Ni-Cu30-Al6-Cr5) for bondcoat were used as powder feedstock material. Details of the coating process, parameters and feedstock materials can be found in Ref 40.

Thermal Cycling

The coatings were thermally tested with laser cycling experiments. Cylindrical CuCr1Zr substrates with a height of 50 mm and a diameter of 20 mm were coated on the front end. The coating surface is heated with a 3.3 kW diode laser; the laser power is controlled by a two-color pyrometer to get a constant surface temperature. Every heating cycle starts with maximum laser power until the set point temperature is reached. The laser beam is divergently widened with a special optics to produce a broad focal point. In the current work, a working distance (between laser optics and coating surface) of 200 mm is used, where

the focal point is approximately 10 mm in diameter. The resulting heat flux density reaches approximately 30 MW/m² and leads to a large thermal gradient in the sample during the first second of each laser cycle, even without cooling. After each cycle, the samples are automatically quenched in water to simulate the post-cooling of the engine after shutdown. A detailed description of the laser test bed can be found in Ref 26, 61.

The thickness of the coating system including bondcoat and topcoat was varied from 90 µm to 300 µm, while the bondcoat thickness was kept constant at 45 µm.

Tensile Tests on Coated Samples

To determine the critical strain for the growth of vertical cracks at room temperature, tensile tests were performed. The critical strain where cracks in the coatings start growing depends on the morphology of the coating surface since stress concentrations at sharp edges may reduce the critical strain significantly. To account for these stochastic microstructural effects, a large probing volume should be used to investigate critical strains for crack initiation. For this purpose, coated tensile specimens were tested. Flat tensile test specimens were machined from a CuCr1Zr sheet and coated with the Rene80 topcoat material. Due to the missing heat loads in the experiments and the fact that vertical cracks originate from the surface of the Rene80 topcoat, a bondcoat is not necessary here. The coated tensile specimens were continuously loaded in a tensile test at room temperature, and the strains on the coating surface were measured with an optical strain sensor GOM Aramis 5 M. The local strains are measured by defining small rectangle-shaped facets on the surface and optical tracking of the edges of these facets. Figure 2 shows the evolution of the strains on the coating surface at different steps of the tensile test. If a crack runs through the coating, the rectangular facets are deformed due to the crack opening and a local increase in the strain is detected for those facets. This is shown in Fig. 2 in the left upper area of the images.

The cracks grow at strains where the copper specimen is not linear elastic any more. Due to the relatively low work hardening of the CuCr1Zr alloy, the strain distribution in the specimen becomes inhomogeneous (see Fig. 2a). Thus, the critical strain for crack growth is not equal to the overall strain of the whole specimen. Instead, the critical strain is determined from the optical strain measurements along the marker in Fig. 2(a), where the first local strain maxima due to crack growth were detected.

FEM Simulations

To elucidate the failure mechanisms observed in the thermal cycling experiments and to predict possible coating

failure in rocket engine application, finite element simulations were carried out using Abaqus Standard (Ref 62). The models are described in the following sections.

Material properties for the CuCr1Zr substrate material were taken from Ref 63–70. For the nickel jacket, material properties from Ref 71, 72 were used. The parameters for the coatings were taken from own measurements which are already reported in Ref 10, 61, 73 and from Ref 46. Except for the elastic buckling simulations, elastic-plastic material behavior using isotropic hardening was modeled for all materials.

Creep was not modeled although the material is expected to creep rapidly at the high temperatures. But the plasticity data were obtained from quasistatic compression tests, where the material is expected to creep at high temperatures. Thus, it could not be differentiated between plastic strain and creep strain in the plasticity data for the material. Furthermore, the remaining elastic strain in the coatings at high temperatures is small (0.1%) compared to the plastic strain (> 1.5%) (see “[Thermomechanical Loads on the Coatings](#)” section). Thus, explicitly allowing for creep in the simulations has a negligible influence in the modeling results, which has also been shown in simulations with a parameter study on a simple Norton creep law.

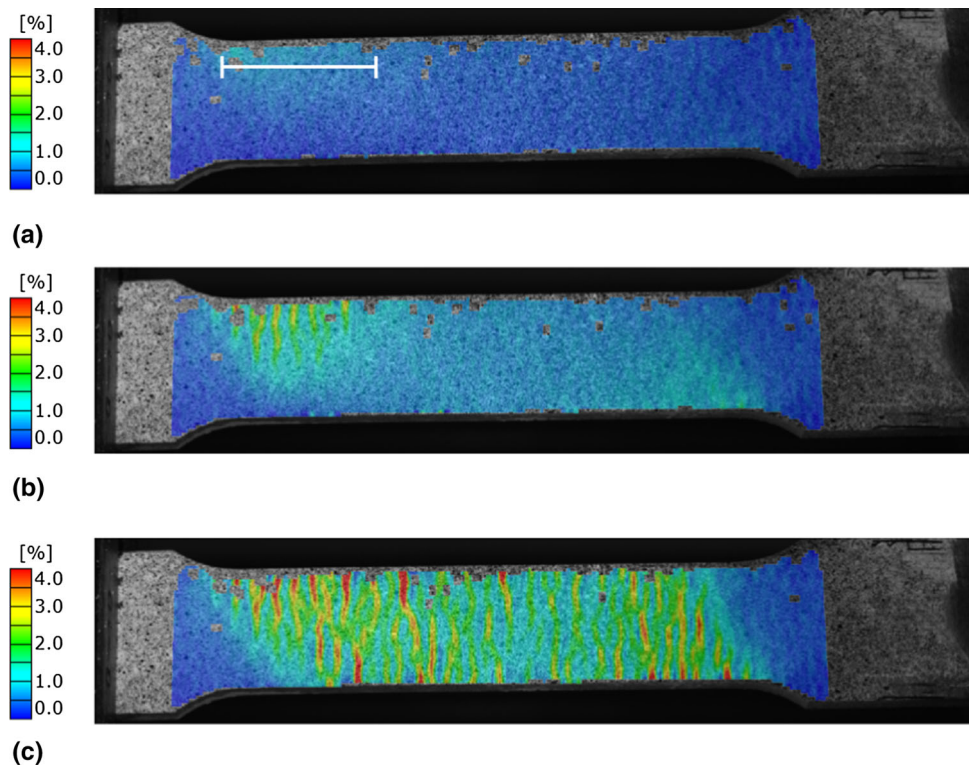
FEM Model of the Laser Sample

The laser sample was modeled with an axisymmetric model which was meshed with a minimum of 2300 elements, depending on the coating thickness. The thickness of the bondcoat was constant at 45 µm, and the overall coating thickness including bondcoat and topcoat was varied from 90 µm to 300 µm, according to the laser cycling experiments. Axisymmetric quadrangular-shaped quadratic elements with hybrid formulation and reduced integration were used. For details of the model, see Ref 61.

The heat flux from the laser radiation is applied to a circular area with the diameter of the laser spot. To control the heat flux in order to get a constant surface temperature similar to the experiment, a user subroutine UAMP (Ref 62) was developed. The user subroutine models the temperature measurement with the two-color pyrometer so that local overheating due to interface delaminations had a realistic influence on the measured temperature and thus the heat flux. For this purpose, the electromagnetic emission M_i at the measurement wavelengths λ_i of the pyrometer ($\lambda_1 = 750$ nm; $\lambda_2 = 1100$ nm) is calculated at each node on the coating surface in the FEM model using the following equation (Ref 74):

$$M_i = \frac{2\pi hc^2}{\lambda_i^5} \cdot \frac{1}{\exp\left(\frac{hc}{k\lambda_i T}\right) - 1}$$

Fig. 2 Strains on the coating surface at different steps of the tensile test. The white bar in the first image indicates the range for the determination of critical strain in this area as described in the text. (a) Whole specimen strain: 0.36%. (b) Whole specimen strain: 0.80%. (c) Whole specimen strain: 1.66%



where h is the Planck constant, c the speed of light in vacuum, k the Boltzmann constant and T the temperature. The emission M_i is integrated over the whole coating surface (the measurement area of the pyrometer) for each measurement wavelength, and the quotient of both values is calculated.

With a Newton-Raphson algorithm, the apparent surface temperature as measured by the pyrometer is determined from the quotient of the emission. The apparent pyrometer temperature is then used to control the laser power using a PID controller.

On some samples, the temperature gradient in the modeled laser sample was compared to measured values from internal thermocouples in the experiment to validate the simulations. A good agreement between the modeled and the measured temperatures was observed (Ref 61).

Modeling of Crack Propagation at the Substrate/Coating Interface

To determine the energy release rate due to interface crack propagation in the laser cycling experiments, a small separation was modeled at the substrate/coating interface. At the tip of the separation, both crack surfaces were tied along an area with the width of one element (10 μm). In a subsequent step, the surface to surface interaction at the crack tip was released to model crack propagation, and the

change of stored elastic energy in the whole model was calculated.

A whole laser cycle was thermo-mechanically modeled for each investigated crack length. Thermal conduction through the interface separation was allowed in cases where thermal expansion leads to a crack closure. Radiation was not modeled since the radiation heat flux is negligible small compared to the heat flux by thermal conduction (Ref 61). Verification simulations showed nearly no difference between modeling with and without interface radiation.

In a restart analysis of the thermo-mechanical modeling, the crack propagation was carried out at certain time steps of the laser cycle to determine different energy release rates during the laser cycle.

Although no dedicated buckling computation was performed in these simulations, the inhomogeneous heating and thus inhomogeneous deformation of the separated part of the coating were a sufficient perturbation to cause buckling in the FEM model if the strain energy was large enough, see Fig. 3.

Modeling of Buckling

To investigate fundamentals of coating buckling, a simplified model with a 180- μm -thick monolayer was created. The coating was axisymmetric with a radius of 10 mm, similar to the coatings in the laser experiments. The

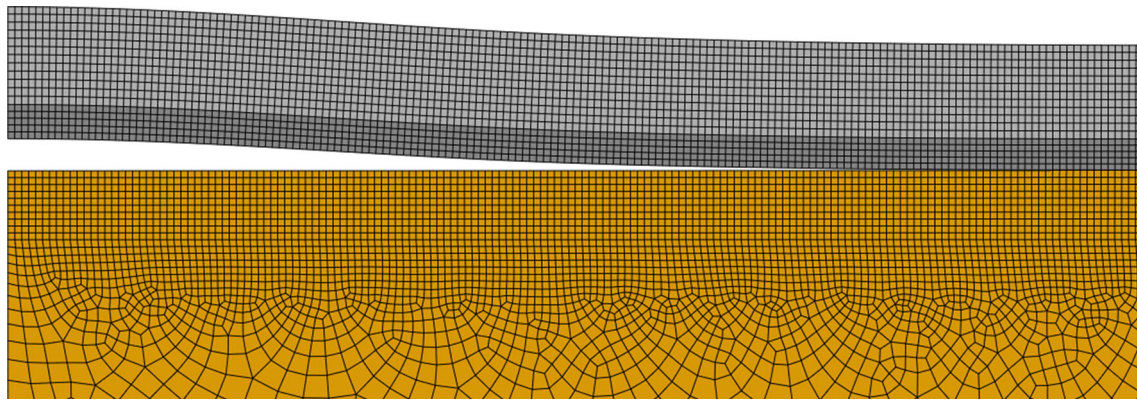


Fig. 3 Simulation of laser cycling experiments with a 180- μm -thick coating system: buckling of the coating during heating. The colors indicate the three different material sections substrate, bondcoat and topcoat

substrate was not modeled. Instead, the coating was clamped on the bottom side with a displacement boundary condition. Simple, temperature-independent material parameters were used for the coating: Young's modulus was 155 GPa, Poisson's ratio 0.3 and the coefficient of thermal expansion $13 \times 10^{-6}/\text{K}$. For plastic buckling, a yield stress of 1000 MPa was used. The coating was assumed to be stress-free at the initial state. Afterward, the temperature was increased using a predefined temperature field to obtain compressive stresses from the thermal expansion of the coating material. A delamination was modeled by deactivating the boundary condition in an area in the center of the bottom side of the coating, and the buckling was analyzed in the following two ways.

On the one hand, to investigate whether the structure buckles, or which load is required for buckling, a linear perturbation analysis was performed in Abaqus, where a predefined loading pattern, for example, a temperature field, is multiplied with a variable factor. Different values of this multiplier are then calculated by the software for each buckling mode. For example, when the multiplier of the first mode (other modes were not relevant for the present study) is greater than 1, the structure will not buckle under the predefined load pattern. A multiplier of less than 1 indicates that the structure will buckle at the predefined loads (Ref 62).

On the other hand, to investigate the energy release or the deflection of the buckled structure, a perturbation was applied with a forced displacement boundary condition in the center of the detached part of the coating. The displacement was incrementally increased, and the energy (elastic strain energy and plastic dissipation energy in the case of plastic behavior) was calculated for the model at each increment. To eliminate edge effects, the energy of an area with 2 times the diameter of the buckled structure was

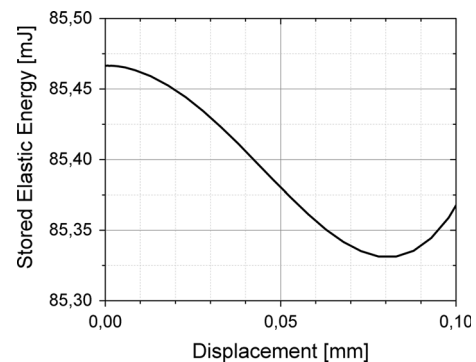


Fig. 4 Stored elastic energy vs. displacement in the thickness direction of the center of a buckled plate after temperature increase of 400 K

analyzed. Figure 4 shows the energy versus the displacement in thickness direction of the simplified model of a coating after a temperature increase of 400 K. In this example, the energy reaches a minimum at a displacement of 0.08 mm. Thus, the buckling amplitude is 0.08 mm, and the energy release due to buckling is 0.13 mJ. In cases where the coatings did not buckle, the energy minimum was at zero displacement, and the bending of the coatings did not lead to a positive energy release.

Coating Damage by Vertical Cracks

Creep and plastic deformation due to large compressive strains at high temperature may lead to tensile strains in the coatings during the subsequent cooling phase (see “[Thermomechanical Loads on the Coatings](#)” section). These strains, if large enough, may cause growth of vertical cracks starting at the coating surface (Ref 10, 40).

Vertical Cracks in Laser Cycling Experiments

For the examination of vertical cracks in the laser cycling experiments, other failure mechanisms like buckling (see “Coating Damage by Buckling” section) have to be avoided. Thus, the coating adhesion was enhanced by a diffusion heat treatment. This post-spray treatment made it possible to investigate the sensitivity to vertical cracking up to surface temperatures of 1112 K in the laser cycling experiments. The results of these experiments are summarized in Fig. 5: At the maximum possible temperature of 1112 K, vertical cracks were observed after 20 cycles at coating thicknesses of 180 μm and above. At lower surface temperatures or lower coating thicknesses, neither vertical cracks nor any other damage mechanisms could be observed.

Figure 6 shows cut views through typical vertical cracks in a 180-μm-thick and a 300-μm-thick coating. In both cases, the cracks run through the upper half of the coating and stop before reaching the bondcoat material. A kinking of the crack can be observed at the crack tip in some cases, as shown in Fig. 7. This crack kinking may be caused by a residual bending moment, since the highest tensile strains occur near the coating surface, see also “FEM Simulations of Laser Cycling Experiments” section. It may also be due to the inhomogeneous microstructure exhibiting flattened splats, making crack propagation along splat interfaces easier in a direction parallel to the coating surface.

Critical Loads for Vertical Cracks

To elucidate the mechanisms of crack growth and to predict coating failure by vertical cracks in finite element simulations, it is important to know the critical strain where the cracks start growing. This critical strain was determined in tensile tests of coated copper samples according to “Tensile Tests on Coated Samples” section. To determine

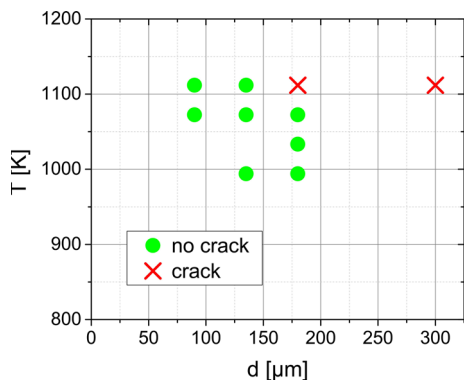
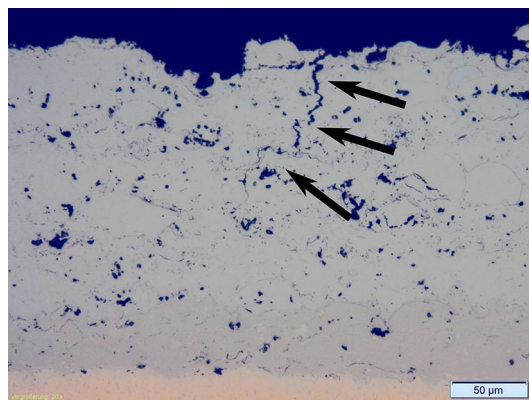
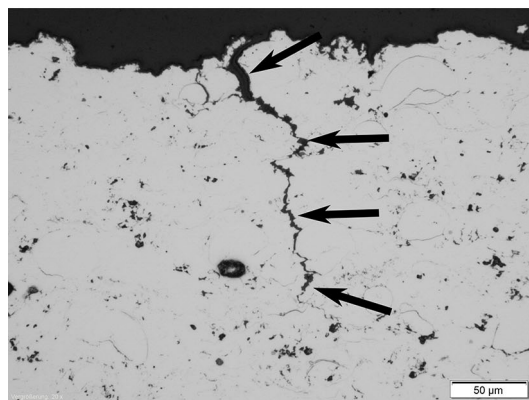


Fig. 5 Failure Map: vertical cracking of coatings with a different thickness d and surface temperature T (after diffusion heat treatment to prevent buckling)



(a)



(b)

Fig. 6 Vertical cracks indicated with arrows after 20 cycles in the laser experiment with 1112 K surface temperature. (a) 180 μm coating thickness. (b) 300 μm coating thickness

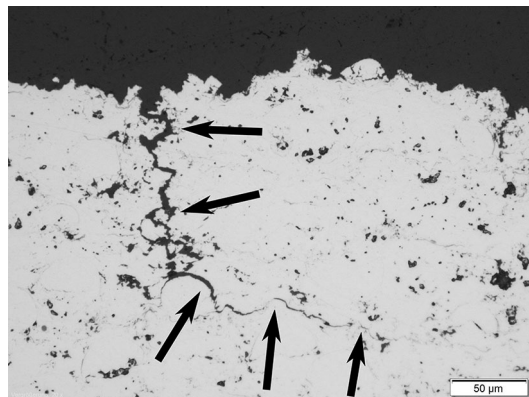


Fig. 7 Crack kinking (see arrows) in a 300-μm-thick coating after laser cycling

the onset of crack growth, the maximum local strain from the measurements is plotted in comparison with the minimum and the mean value in Fig. 8. The overall strain on the horizontal axis is measured along the small segment marked in Fig. 2(a), according to “Tensile Tests on Coated Samples” section.

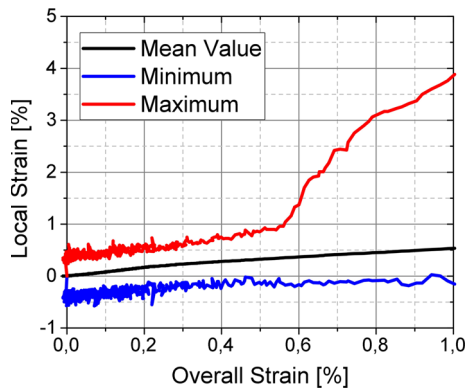


Fig. 8 Statistics of the local strains compared to the overall strain along the segment marked in Fig. 2(a)

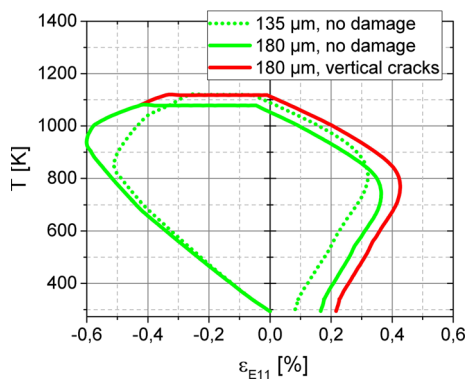


Fig. 9 Elastic strains from FEM simulations near the coating surface in the center of the laser spot during laser cycling with different coating thicknesses and temperatures. The green curves indicate a laser cycle where no damage was observed in the corresponding experiment; the red curve indicates data where vertical cracks were observed in the experiments

From the maximum value of the strains in Fig. 8, the onset of the crack growth can be identified at a total strain of approximately 0.55%.

FEM Simulations of Laser Cycling Experiments

To elucidate the loads in the coatings during the laser cycling experiments, finite element simulations were carried out as described in “FEM Model of the Laser Sample” section. Figure 9 shows the elastic strains at a point near the coating surface in the center of the laser spot during the first laser cycle for different experiments. The evolution of these strains has been discussed in detail in “Thermomechanical Loads on the Coatings” section: During heating, the coatings exhibit elastic compressive strains which are reduced due to plasticity at higher temperatures. The resulting plastic strains lead to residual elastic tensile strains after the cooling cycle.

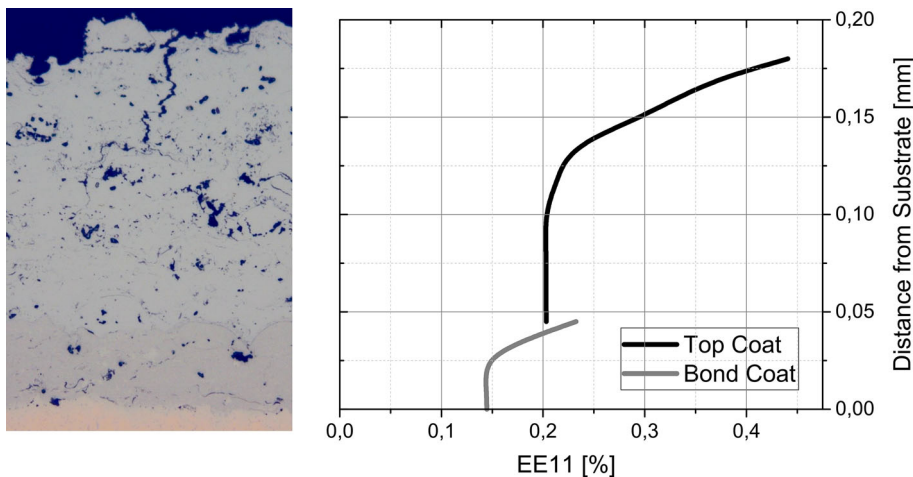
The diagram in Fig. 9 shows that coatings with a thickness below 180 μm exhibit less elastic strains in laser experiments with the same surface temperature. This is caused by less thermal insulation by the thinner coatings and thus a faster heating and larger thermal expansion of the copper substrate. The influence of the surface temperatures can be seen, for example, at a coating thickness of 180 μm in Fig. 9: Lower temperatures lead to less plastic deformation (due to the larger yield strength at lower temperature) and thus less tensile strains during cooling.

For the investigation of critical loading conditions leading to vertical cracks, the finite element simulations can be compared to the experiments. According to the three experiments modeled in Fig. 9, a tensile strain of 0.36% is tolerable without vertical cracks. In contrast, a critical strain for crack growth at 0.55% was determined in the tensile tests (“Critical Loads for Vertical Cracks” section). The difference can be explained with residual strains from the coating process which overlay the strains in the tensile tests. The residual compressive strains can be neglected in the simulation of the laser cycling experiment since the coatings yield during heating so that the stress state at high temperature becomes independent of the prior history. Measurements of the residual strains in the coatings by the bore hole method (Ref 75) showed residual compressive strains in the coatings of up to 0.1–0.2% after the coating process. The measured value of the residual strains explains the difference between critical strain for cracking in the laser experiments and in the tensile tests.

The cracks stop before reaching the bondcoat, see Fig. 6. An analysis of the elastic strain profile through the coating during cooling down in Fig. 10 shows that the tensile strains are maximal near the coating surface where the highest temperatures were reached. Below the coating surface, lower temperatures led to less compressive strain and less plastic deformation during heating and thus less elastic tensile strain during cooling. Due to the different material properties like yield strength and coefficient of thermal expansion of topcoat and bondcoat, the elastic strain is discontinuous at the interface and is even lower in the inside of the bondcoat. Apparently, the small strains in the coating system below the surface are not large enough to keep the crack running toward the substrate.

The strain profile in Fig. 10 leads to a residual bending momentum in the coating, which may cause the cracks to kink, as mentioned in “Vertical Cracks in Laser Cycling Experiments” section. Such bending-induced cracks, also known as edge delaminations, are a typical interface failure in ceramic TBC systems and were investigated in more detail, for example, in Ref 76, 77.

Fig. 10 Micrograph of the cracked coating (same as shown in Fig. 6 left) and elastic strain profile during cooling at the point of time where the strain is maximal at the surface, determined in FEM simulations of a 180- μm -thick coating with 1112 K surface temperature in the laser experiment



Failure in the Combustion Chamber and Design Guidelines

According to previous FEM simulations of a coated combustion chamber segment (Ref 78), as the strains are essentially relaxed to zero in the hot state, total tensile strains of up to 2.2% can be expected in rocket engine application of the coatings (see Fig. 1). These strains are above the critical strains (0.36%) determined in the previous sections, and the coatings can be expected to crack vertically.

For the coating design in rocket engines, it is of great importance to predict whether the cracks reach the substrate or not. On the one hand, crack propagation into the substrate can induce critical damage of the cooling channels and even a failure of the whole rocket engine. On the other hand, the cracks may kink upon reaching the substrate and propagate along the substrate/coating interface in Mode I (bending moment caused by the stress gradient) or Mode II (tensile loads in the coating).

Near the substrate/coating interface, lower temperatures and thus less thermal expansion and less plastic deformation compared to the coating surface can be expected. As seen in the simulations of the laser experiments (Fig. 10), the resulting tensile strains are lower inside the coating than near the hot gas surface, and the cracks may stop upon reaching the substrate, even in the combustion chamber. For coating design, the strain profile in the combustion chamber could be compared to the strain profile from the laser experiments to predict whether the cracks may propagate into the substrate. However, future work has to focus on a more detailed investigation of cyclic crack growth and the determination of critical stress intensity factors.

Coating Damage by Buckling

During heating, the coatings exhibit large compressive strains (“[Thermomechanical Loads on the Coatings](#)” section). If these strains exceed a critical value, depending on the weakness of the substrate/coating interface, the coatings may tend to buckle (Ref 10, 40).

Critical Loads for Buckling

The buckling phenomenon has been investigated in detail by Hutchinson, Evans et al., Ref 79-82: If the coating is under compressive load parallel to the surface and if the coating is detached from the substrate, a critical stress can be calculated where the coating becomes unstable and buckles. Assuming that the area of detachment is circular, the coating can be modeled as a clamped circular plate according to the von Karman plate theory (Ref 83) (for details of the solution of this nonlinear plate theory see Ref 82). According to Hutchinson et al. (Ref 82), the critical stress σ_c where the coating starts to buckle can be calculated by

$$\sigma_c = 4.894 \cdot \frac{E}{1 - \nu^2} \cdot \frac{d^2}{l_c^2}, \tag{Eq 4.1}$$

assuming that $l_c \gg d$. E is the Young’s modulus, ν is the Poisson’s ratio of the coating, d is the coating thickness and l_c is the critical length of the buckled plate, in this case the diameter of the detached area.

For stresses $\sigma > \sigma_c$, the height δ (maximum distance from substrate to coating downside) of the buckled coating can be approximated by the following equation (for a Poisson’s ratio of 0.3) (Ref 82):

$$\delta \approx d \cdot 1.3808 \cdot \sqrt{\frac{\sigma}{\sigma_c} - 1} \tag{Eq 4.2}$$

Table 1 Multiplier of the predefined load pattern (see “Modelling of Buckling” section) from the buckling analysis of a thermally loaded coating with different diameters of delamination, l_c , with constant temperature and with a thermal gradient

l_c , mm	Thermal gradient	Constant temperature
2.5	1.2876	1.2873
5.0	0.3504	0.3504
10.0	0.0909	0.0909

This approximation is correct for small differences of σ and σ_c ; for larger values of σ , δ is overestimated. For stresses of $\sigma = 10 \cdot \sigma_c$, for example, δ is overestimated by 7% (Ref 82).

Influence of Strain Gradient

In reality, due to the large thermal gradient, the strain is not constant over the coating thickness, and a strain gradient and thus a bending moment have to be considered. The influence of this bending moment can be analytically estimated using simple double-clamped Euler column: In the solution of the differential equation (see Ref 83), the additional bending moment vanishes when inserting the constant boundary conditions at the fully clamped edges. Thus, the critical Euler load for buckling is independent of this additional bending moment.

For the clamped circular plate, this calculation becomes nonlinear and cannot be solved analytically (Ref 82). Thus, it was elucidated in FEM simulations whether the assumption from the Euler column is also valid for the circular plate.

For this purpose, a 180- μm -thick, axisymmetric coating was investigated with linear perturbation according to “Modelling of Buckling” section. A temperature increase of 1000 K compared to the initial temperature was applied. On the one hand, a constant temperature in the coating was defined; on the other hand, a thermal gradient of 2 K/ μm was defined in a way that the average temperature in the coating was 1000 K above the initial temperature.

Table 1 shows the load multiplier where the structure buckles from the thermal buckling analysis according to “Modelling of Buckling” section. For each delamination size, the multipliers are nearly independent of the (relatively large) thermal gradient. That means the critical average temperature (and thus strain) for buckling is similar with and without a temperature (and thus strain) gradient.

To compare the simulation results with the analytical approach, the resulting critical strains for buckling are shown in Table 2 together with the critical strains

Table 2 Critical buckling strain ε_c from the buckling analysis of a thermally loaded coating with different diameters of delamination, l_c , compared to the analytical approach according to Eq 4.1

l_c , mm	Simulation	Equation 4.1
2.5	0.0239	0.0279
5.0	0.0065	0.0070
10.0	0.0017	0.0017

calculated according to Eq 4.1 for each delamination length. For a delamination length of 2.5 mm, the critical strains differ by 14%, whereas for larger lengths, the difference decreases to 3% at $l_c = 10$ mm. This deviation can be explained by the fact that Eq 4.1 is only valid for $l_c \gg d$ (Ref 82).

The maximum elastic compressive strain in the laser cycling experiments, averaged over the coating thickness, is less than 0.5% for a 180- μm -thick coating. According to the calculations above, an interface separation with a diameter of more than 5 mm is necessary for a buckling of the coating.

Plastic Buckling

The analytical approach is only valid for elastic material behavior. For plastic buckling, the energy can be considered: The structure buckles if the total energy in the buckled state is less than the energy in the unbuckled state. In the unbuckled state, the strain energy results just from the elastic compression of the plate. In the buckled state, on the one hand some of the elastic strain energy is released due to elongation of the plate; on the other hand, the structure is bent which results in additional plastic and elastic deformation energy. The stored energy in the bent state is less in the case of plastic deformation. Thus, the energy release due to buckling is larger with plastic deformation, which results in lower critical buckling strains ε_c .

To investigate the effect of plastic deformation on the energy release, FEM simulations with elastic as well as elastic-plastic material behavior were performed on the model with forced displacement according to “Modelling of Buckling” section. The energy release rate of both materials was calculated for different initial in-plane strains; the results are plotted in Fig. 11: The energy release due to buckling of the elastic plate is > 0 for elastic strains larger than 0.67%, whereas the plate with plastic material behavior has a positive energy release at just $\varepsilon_E > 0.59\%$.

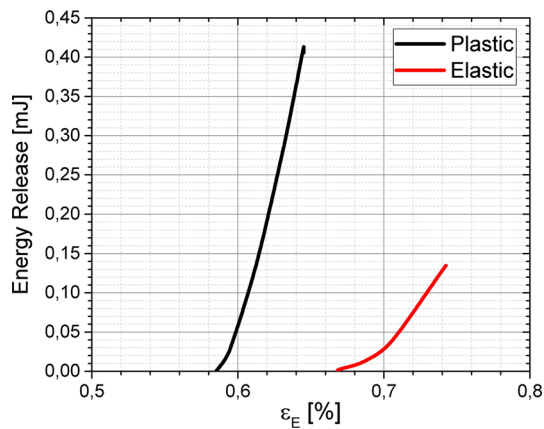


Fig. 11 Energy release due to buckling of a 180- μm -thick coating with an initial delamination with $l = 5$ mm depending on the elastic strain (homogeneous load in the coating): simulations with elastic and with elastic-plastic material behavior

The Role of Interface Delamination

The analysis above shows that an interface separation with a length in the order of magnitude of millimeters is necessary to cause buckling of the coatings. Since the largest interface separations after the coating process are in the order of magnitude of 10 μm , the growth of these separations during thermal cycling up to the critical length has to be elucidated.

Initiation of Interface Cracks

In previous work, it has been shown that small interface cracks can form in the roughness profile of the substrate/coating interface due to thermal mismatch stresses (Ref 12, 13, 39, 84). The coefficient of thermal expansion (CTE) of the copper substrate is, for example, $2\text{--}5 \times 10^{-6}/\text{K}$ larger than the CTE of the bondcoat (Ref 10), which causes thermal strain differences of up to 0.25%. During heating, this results in compressive stresses near the hills and tensile stresses in the valleys of the roughness profile, see Fig. 12. The tensile stresses may induce cracks or crack growth at existing imperfections, whereas the compressive stresses may relax at high temperature and cause tensile stresses in the tips of the roughness profile during cooling down. Thus, thermal cycling will lead to cyclic crack growth. This thermal cycling effect on interface cracks has been investigated in detail analytically and numerically by Evans et al. (Ref 85) on a wavy interface between a metallic substrate and an oxide layer.

Small Interface Cracks Grow Together

Once a crack has formed in a hill or valley of the roughness profile, the stress intensity factor increases, and subsequent

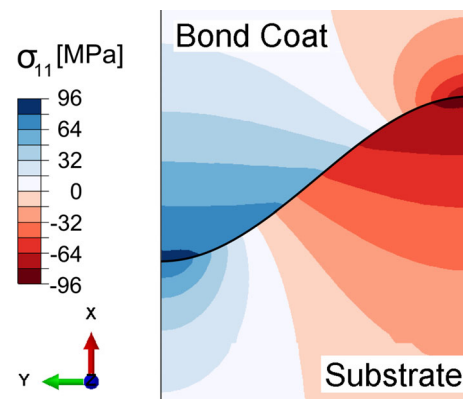


Fig. 12 Interface stresses due to thermal mismatch at an interface temperature of 813 K between a CuCr1Zr substrate and a NiCuCrAl bondcoat (Ref 10)

loading leads to a crack growth. Bäker and Seiler Ref 86, for example, performed simulations with a sinusoidal-shaped interface between two materials with different coefficients of thermal expansion (in this case a ceramic coating and a metallic substrate). They show that the cracks may grow even into areas aside the tips and valleys. These cracks may grow together and become larger delamination cracks.

The mechanisms of delamination crack initiation and growth have not been addressed yet in the finite element modeling in the present work because the modeling of these effects will require complex multiscale simulations. Furthermore, the stochastic shape of the interface leads to several side effects. Thus, empirical data have been considered to define critical interface temperatures at which crack growth becomes relevant. To determine the critical temperature for the combination CuCr1Zr substrate/NiCuCrAl bondcoat, laser cycling experiments were carried out previously with a low heat flux, so that buckling was avoided (Ref 10). It was found that an interface temperature greater than 973 K leads to a measurable increase in interface delaminations after 20 cycles. At 973 K and below, no significant crack growth could be observed in the laser cycling experiments. Above this temperature, interface cracks grow during thermal cycling as long as the temperature and hold time are sufficiently low to prevent an increase in coating adhesion and interface fracture toughness due to interdiffusion. For example, for the coating system investigated in this work, an accumulated hold time of 40 s at an interface temperature of ≈ 1273 K was sufficient to form a diffusion layer which prevents interface crack growth during laser cycling experiments (Ref 10, 40). It has to be noted that, during the first few laser cycles, the enhanced coating adhesion due to diffusion may not be sufficient, and interface cracks may grow until the diffusion processes increase the adhesion in

further laser cycles. This is especially important when larger heat fluxes in the experiments lead to larger thermoshocks during heating as in the experiments in the present work.

Growth of Large-Scale Interface Delaminations

If the crack length is larger than the coating thickness, another effect becomes relevant when a heat flux is applied: The heat flux through the crack diminishes, which results in a local overheating of the coating above the crack. This results in larger thermal expansion and thus larger compression strains in the detached part of the coating that causes a driving force for Mode II crack propagation.

The energy release rate during this crack growth has been derived from FEM simulations of a 180- μm -thick coating in laser cycling experiments (surface temperature of 1118 K) with different initial crack lengths, according to

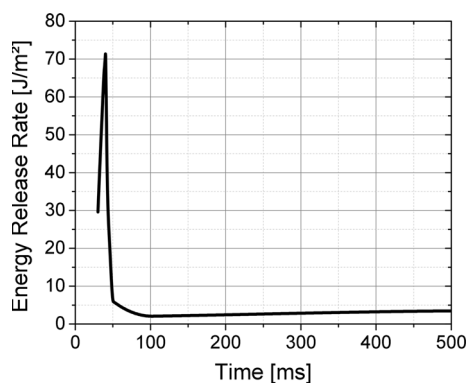


Fig. 13 Energy release rate of a 180- μm -thick coating with an initial crack radius of 0.5 mm during a laser cycle with 1118 K surface temperature

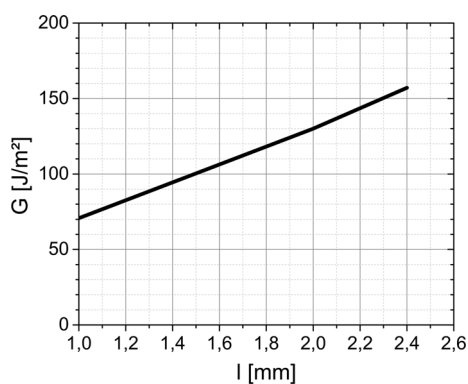


Fig. 14 Energy release rate compared to the initial crack length l during interface delamination growth due to local overheating of the detached coating during laser cycling: FEM simulations of a laser sample with a coating thickness of 180 μm and a surface temperature of 1118 K

“Modelling of Crack Propagation at the Substrate/Coating Interface” section. The energy release rate has a transient maximum during the heating phase (Fig. 13) at about 950 K. Above this temperature, the yield strength of the coating decreases rapidly (Ref 73), which results in increasing plastic strain and decreasing elastic strain and thus decreasing stored elastic energy in the coating.

The maximum energy release rate G during heating is plotted in Fig. 14 for a different initial crack length l . G increases with crack length, since the temperature and consequently the elastic energy per volume of the coating above the crack increase. At a crack length of 3 mm, the coating in the simulation buckled.

A critical energy release rate for crack propagation at the substrate/coating interface is not known yet. But the increasing energy release rate with increasing crack length shows that once a critical length is exceeded, a further crack propagation and thus buckling are very likely.

Buckling in Laser Cycling Experiments

Laser cycling experiments for the investigation of buckling were carried out on coatings without any post-spray diffusion heat treatment. The cross section of a buckled coating is exemplarily shown in Fig. 15 for a 180- μm -thick coating. The results of the buckling investigation in the laser experiments are displayed in Fig. 16.

Coatings with a thickness of 300 μm failed even at surface temperatures below 1000 K by large-scale delamination. A differentiation between delamination cracks and buckling was not possible here. Furthermore, large interface delaminations due to the large heat load on the samples during coating application led to a vague interface damage even before laser cycling. Thus, a distinct investigation of buckling of the 300- μm -thick coatings was not possible.

For coatings with 180- μm thickness, buckling could be observed at surface temperatures of 1038 K or above. Here, two opposing effects influence the buckling: On the one hand, the maximum surface temperature has no influence on the maximum compressive strains in the coatings during heating in the first cycle, as seen in the FEM simulations in Fig. 17: The elastic compressive strains in a 180- μm -thick coating during heating exhibit a maximum at 950 K. At



Fig. 15 Cross section of a coating which buckled during laser cycling. Coating thickness: 180 μm , surface temperature: 1118 K

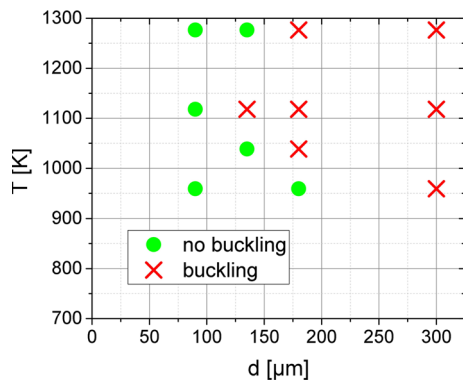


Fig. 16 Failure map: buckling of coatings with a different thickness d and surface temperature T . Different from the results shown in Fig. 5, no heat treatment was performed to improve coating adhesion

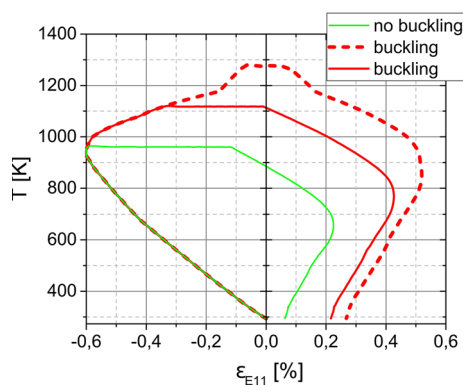


Fig. 17 Elastic strains from FEM simulations near the coating surface in the center of the laser spot during laser cycling of a 180- μm -thick coating with different surface temperatures. The green curves indicate a laser cycle where no damage was observed in the corresponding experiment; the red curve indicates data where the coating buckles

higher temperatures, the coating yields and the elastic compressive strains are reduced. An increase in the surface temperature leads to a further reduction in the elastic strains due to the lower yield strength, and thus, larger tensile strains are reached after cooling down (see also the discussion in “FEM Simulations of Laser Cycling Experiments” section). Consequently, subsequent laser cycles lead to less elastic compressive strains compared to the first cycle (see also Ref 39). The larger the surface temperature is, the lower the compressive strain is in the second and following cycles.

On the other hand, higher surface temperatures cause the growth of interface delaminations. This effect plays a major role in the buckling behavior of the 180- μm -thick coatings and explains why buckling was observed at 1038 K although the largest compressive strains occur in experiments with lower temperatures: Below 1038 K surface temperature, the interface temperature is lower than the critical temperature for delamination crack growth

(973 K, see “Small Interface Cracks Grow Together” section). Without these interface cracks, buckling of the coatings is not possible (“The Role of Interface Delamination” section).

At 135 μm coating thickness, buckling was observed only at surface temperatures of 1118 K. Above 1118 K surface temperature, plastic yield leads to less compressive strains during subsequent cycles compared to experiments with lower surface temperatures (see above). Compared to the 180- μm -thick coatings, the thermal insulation by the 135- μm -thick coatings and thus the temperature difference between coating and substrate are less. This causes a reduction in compressive strains in the coatings which is sufficient to prevent buckling above 1118 K surface temperature. At lower surface temperatures, the strains were not reduced; however, below 1118 K surface temperature, the damage by delamination cracks at the interface was less due to the lower interface temperature, and buckling could be prevented.

Coatings with a thickness of 90 μm did not buckle in the experiments, although large interface cracks could be observed at temperatures above 1100 K. A reason that the coatings did not buckle is the relatively low compressive strain compared to thicker coatings due to a faster heating and thus larger thermal expansion of the substrate, caused by the low thermal insulation of the thin coatings.

In many cases, at least two cycles are necessary for the coatings to buckle. However, the moment of buckling is not reproducible: For example, 180- μm -thick coatings buckled with the same laser cycling parameters after 1, 2 or 6 cycles. This may be caused by the stochastic shape of the substrate/coating interface: The roughness profile and imperfections at the interface have a great influence on interface crack growth.

However, in one example the coating buckled even in the first cycle, the results show that mostly a certain number of thermal cycles are necessary to produce interface separations which are large enough to induce buckling, as discussed in “The Role of Interface Delamination” section.

The diameter of the interface separation of the buckled coatings with 180 μm thickness was approximately 3.2 mm and in good agreement with the critical crack length for buckling determined in the FEM simulations in “Growth of Large Scale Interface Delaminations” section, where a critical crack length of 3.0 mm was calculated. One reason for the larger crack length observed in the experiments is a crack growth after buckling, as investigated in detail by Hutchinson et al. in Ref 79. Furthermore, the FEM simulations may exhibit some error due to inevitable simplifications of the model. Overlying residual compressive strains after coating application (see “FEM Simulations of Laser Cycling Experiments” section) have

only an influence during the first laser cycle. Plastic yield at high temperature leads to elastic strains independent on residual compressive strains.

Thermal History Influence on Buckling Sensitivity

When exposed to high temperatures, diffusion processes may enhance the coating adhesion and, thus, hinder crack growth along the interface between coating and substrate. Thus, interface cracks may not grow to the critical length for buckling according to “[Small Interface Cracks Grow Together](#)” section. This effect has been investigated by a diffusion heat treatment of the coated samples prior to laser cycling experiments.

The experiments showed that, at a coating thickness of 180 μm , a diffusion heat treatment of 0.5 h at 773 K was sufficient to prevent the coating from buckling at a surface temperature of 1112 K, although in the center of the laser spot, the interface between coating and substrate was damaged by delamination cracks along an area with a diameter of approximately 1 mm. Between these cracks, the coating was still adhering at small areas. The laser power did not show any evidence for rapid crack growth or buckling.

After a heat treatment of 6 h at 973 K, the coatings showed neither buckling nor delamination cracks even after 20 laser cycles at 1112 K. This heat treatment was successfully used to prevent buckling in the experiments for the investigation of vertical crack growth in “[Coating damage by Vertical Cracks](#)” section.

The results from the experiments with the post-spray diffusion heat treatment show that it is important to consider the thermal history of the coatings for buckling prediction in future failure models. Furthermore, a diffusion heat treatment could be included to the manufacturing process of the copper liner of the rocket engine to prevent the growth of delamination cracks or buckling of the coating.

Failure in the Combustion Chamber and Design Guidelines

The discussion above shows that a critical interface separation is necessary to induce buckling of the coatings. It was found that it is sufficient to keep the temperature of the substrate/coating interface below a critical value of 973–1073 K to prevent the growth of critical interface cracks. Furthermore, it has to be noted that in rocket combustion chambers, the overheating of the coatings above an interface separation may even lead to a partial melting of the coatings because of the larger heat flux and the fact that the surface temperature in the laser experiments in this study is controlled and in the combustion

chamber not. This makes even delamination cracks smaller than the critical length obtained here for the conducted laser cycling experiments crucial for a coating failure.

Simulations of coatings in a reference combustion chamber show that the maximum interface temperature is below 800 K (Ref 39). In this case, the coatings can not be expected to buckle. Furthermore, the coatings’ adhesion can be enhanced by a diffusion heat treatment, for example for 6 h at 973 K.

Conclusions

Metallic coatings for rocket engines may exhibit two main failure modes when exposed to thermal shocks and large heat fluxes: vertical cracks and buckling. Both are caused by the large thermal gradient resulting from the large heat flux. The failure modes were investigated in the present work in laser cycling experiments, tensile tests and finite element simulations. The main conclusions can be summed up as follows:

Vertical Cracks

- Tensile strains during cooling may induce vertical cracks.
- The tensile strains are caused by plastic yield at high temperatures and subsequent contraction during cooling down.
- Vertical cracks start growing at the coating surface at strains greater than 0.36%.
- The cracks may stop growing before reaching the substrate due to a strain gradient in the coating.

Buckling

- Compressive strains during heating may induce buckling.
- The compressive strains are caused by the different temperatures and thus different thermal expansions of coating and substrate.
- A requirement for buckling is an adequate damage of the substrate/coating interface, e.g., by delamination cracks.
- Small delamination cracks grow due to thermal mismatch stresses at the substrate/coating interface.
- Overheating of the coating above small interface cracks can cause a crack growth and even buckling.
- Buckling was prevented in the experiments by keeping the substrate/coating interface temperature below 1000 K.

- Diffusion processes due to longer heat exposure increase the coating adhesion and increase the critical temperature for substrate/coating interface failure.
- Delamination and thus buckling can be hindered by a post-spray heat treatment. In this work, a heat treatment of 6 h at 973 K showed good results.

Acknowledgments Financial support has been provided by the German Research Foundation (Deutsche Forschungsgemeinschaft—DFG) in the framework of the Sonderforschungsbereich Transregio 40, project D2. Heat transfer coefficients for combustion chamber modeling are provided by Daniel Kowollik from the Institute of Aircraft Design and Lightweight Structures, TU Braunschweig. Residual stresses were measured at Universität Kassel—Department of Materials Engineering. Parts of the laser cycling experiments were performed with assistance of Tim Klatt, Malte Knudsen and José Weiland from the institute for Materials, TU Braunschweig.

References

1. M.J.L. Turner, *Rocket and Spacecraft Propulsion*, Springer, Berlin, 2009
2. L. Winterfeldt, D. B. Laumert, D. R. Tano, D. P. James, F. Geneau, R. Blasi, and D. G. Hagemann, Redesign of Vulcain 2 Nozzle Extension, *AIAA/ASME/SAE/ASEE Joint Propulsion Conference and Exhibit*, 41, 2005
3. L. Ogbuji, A Table-Top Technique for Assessing the Blanching Resistance of Cu Alloys, *Oxid. Met.*, 2005, **63**(5-6), p 383-399
4. F. Hötte, T. Fiedler, M.C. Haupt, P. Lungu, C. V. Sethe, and O. Haidn, Experimental Investigations of Thermomechanical Fluid-Structure Interaction in Rocket Combustion Chambers, *J. Propuls. Power*, 2019. <https://doi.org/10.2514/1.B37439>
5. U. Schulz, K. Fritscher, M. Peters, D. Greuel, and O. Haidn, Fabrication of TBC-Armored Rocket Combustion Chambers by EB-PVD Methods and TLP Assembling, *Sci. Technol. Adv. Mater.*, 2005, **6**(2), p 103-110
6. M. Fassin, D. Kowollik, S. Wulfinghoff, S. Reese, and M. Haupt, Design Studies of Rocket Engine Cooling Structures for Fatigue Experiments, *Arch. Appl. Mech.*, 2016, **86**, p 2063-2093
7. D. Kuhl, J. Riccius, and O.J. Haidn, Thermomechanical Analysis and Optimization of Cryogenic Liquid Rocket Engines, *J. Propuls. Power*, 2002, **18**, p 835-846
8. R. J. Quentmeyer, Thrust Chamber Thermal Barrier Coating Techniques. *NASA Report Technical Memorandum*, 1988, NASA TM-100933
9. P. Jain, S.V. Raj, and K.J. Hemker, Characterization of Nicraly Coatings for a High Strength, High Conductivity GRCo-84 Copper Alloy, *Acta Mater.*, 2007, **55**, p 5103-5113
10. T. Fiedler, *Wärmedämmschichten für Raketentriebwerke*, Niedersächsisches Forschungszentrum für Luftfahrt, Braunschweig, 2018 ((in German))
11. T. Fiedler, T. Fedorova, J. Rösler, and M. Bäker, Design of a Nickel-Based Bond-Coat Alloy for Thermal Barrier Coatings on Copper Substrates, *Metals*, 2014, **4**, p 503-518
12. T. Fiedler, M. Bäker, and J. Rösler, Finite Element Simulation of Thermal Barrier Coatings in Rocket Engines, in *SIMULIA Community Conference*, 2015
13. J. Schloesser, *Mechanische Integrität von Wärmedämmschichten für den Einsatz in Raketentriebkammern*, Der Andere Verlag, Uelvesbüll, 2014 ((in German))
14. L. Pawlowski, *Science and Engineering of Thermal Spray Coatings*, Wiley, Hoboken, 2008
15. R.A. Miller, Current Status of Thermal Barrier Coatings—An Overview, *Surf. Coat. Technol.*, 1987, **30**, p 1-11
16. R. Vassen, F. Cernuschi, G. Rizzi, A. Scivani, N. Markocsan, L. Östergren, A. Kloosterman, R. Mevrel, J. Feist, and J. Nicholls, Recent Activities in the Field of Thermal Barrier Coatings Including Burner Rig Testing in the European Union, *Adv. Eng. Mater.*, 2008, **10**(10), p 907-921
17. X.Q. Cao, R. Vassen, and D. Stoeber, Ceramic Materials for Thermal Barrier Coatings, *J. Eur. Ceram. Soc.*, 2004, **24**, p 1-10
18. A. Feuerstein, J. Knapp, T. Taylor, A. Ashary, A. Bolcavage, and N. Hitchman, Technical and Economical Aspects of Current Thermal Barrier Coating Systems for Gas Turbine Engines by Thermal Spray and EBPVD: A Review, *J. Ther. Spray Technol.*, 2008, **17**(2), p 199-213
19. R.J. Quentmeyer, H.J. Kasper, and J.M. Kazaroff, Investigation of the Effect of Ceramic Coatings on Rocket Thrust Chamber Life, in *AIAA/SAE 14th Joint Propulsion Conference*, 1978
20. H. Immich and W. Mayer, Cryogenic Liquid Rocket Engine Technology Developments within the German National Technology Programme. in *AIAA*, 1997
21. H. Immich, J. Kretschmer, and D. Preclik, Technology Developments for Cryogenic Rocket Engines. in *36th AIAA/ASME/SAE/ASEE Joint Propulsion Conference & Exhibit*, 2000
22. H. Immich, J. Alting, J. Kretschmer, and D. Preclik, Technology Development for Thrust Chambers of Future Launch Vehicle Liquid Rocket Engines, *Acta Astronaut.*, 2003, **53**, p 597-605
23. D. Greuel, D. Suslov, O. Haidn, and K. Fritscher, Thermal Barrier Coatings for Cryogenic Rocket Engines, *AIAA J.*, 2002, **1**, p 4145
24. K. Fritscher, J. Brien, C. Kröder, D. Greuel, and U. Schulz, Application and Testing of EBPVD Thermal BARRIER Coatings for Cryogenic Rocket Systems, in *4th European Workshop Hot Structures and Thermal Protection Systems for Space Vehicles*, 2003
25. A. Golikov and M. Polyanskii, Thermocyclic Testing of Heat-Resistant Coatings at Megawatt Three-Phase Plasmatron, *J. Eng. Thermophys.*, 2008, **17**(4), p 311-319
26. J. Schloesser, M. Bäker, and J. Rösler, Laser Cycling and Thermal Cycling Exposure of Thermal Barrier Coatings on Copper Substrates, *Surf. Coat. Technol.*, 2011, **206**, p 1605-1608
27. W. Schröder, F. Breede, C. Danowski, M. Grilli, M. Hahn, M. Hosters, M. Klaus, D. Kowollik, C. Genin, G. Schiedder, J. Schloesser, V. Tini, T. Wallmersperger, and S. Willems, Sfb transregio 40: Schubdüse, *Deutscher Luft- und Raumfahrtkongress*, 2011 (in German)
28. T. Fiedler, J. Schloesser, J. Rösler, and M. Bäker, Development of a Thermal-Barrier Coating-System for Rocket Combustion Chambers, in *6th European Conference for Aeronautics and Space Sciences*, 2015
29. D.S.C. Kowollik, P. Horst, and M.C. Haupt, Fluid-Structure Interaction Analysis Applied to Thermal Barrier Coated Cooled Rocket Thrust Chamber with Subsequent Local Investigation of Delamination Phenomena, *Prog. Propuls. Phys.*, 2013, **4**, p 617-636
30. L.J. Ghosn and S.V. Raj, Residual Stresses in Thermal Barrier Coatings for a Cu-8Cr-4Nb Substrate System, in *NASA Technical Memorandum*, 2002, 2002-211561
31. S.V. Raj, Blanch Resistant and Thermal Barrier NiAl Coating Systems for Advanced Copper Alloys. *US-Patent*, 2015
32. J.A. Nesbitt, NiCrAlY and CuCr Protective Coatings Tested for Copper-Based Thrust Chambers, *Research and Technology*, 2005, pp. 112-114
33. V. Fedorov, V. Chvanov, F. Chelkins, A. Polyanski, N. Ivanov, I. Lozino-Lozinskaya, and A. Buryak, The Chamber Cooling System of RD-170 Engine Family: Design, Parameters, and Hardware Investigation Data, in *42nd AIAA/ASME/SAE/ASEE Joint Propulsion Conference & Exhibit*, 2006

34. A. Vasin, V. Fedorov, and G. Babaeva, Coating for a Liquid-Propellant Rocket Combustion Chamber. *EU-Patent*, 2005
35. K. Hemker, Microsample Characterization of Coatings for GRCop-84 for High Heat Flux Applications. *NASA Report*, 2003, CR-2003-212200
36. L.U. Ogbuji, Oxidation Behavior of Cu-Cr Environmental Barrier Coatings on Cu-8Cr-4Nb, *Surf. Coat. Technol.*, 2005, **197**(2-3), p 327-335
37. S.V. Raj, L.J. Ghosn, C. Robinson, and D. Humphrey, High Heat Flux Exposures of Coated GRCop-84 Substrates, *Mater. Sci. Eng., A*, 2007, **457**, p 300-312
38. S.V. Raj, C. Barrett, J. Karthikeyan, and R. Garlick, Comparison of the Cyclic Oxidation Behavior of Cold Sprayed CuCrAl-Coated and Uncoated GRCop-84 Substrates for Space Launch Vehicles, *Surf. Coat. Technol.*, 2007, **201**, p 7222-7234
39. M. Bäker, T. Fiedler, and J. Rösler, Stress Evolution in Thermal Barrier Coatings for Rocket Engine Applications, *Mech. Adv. Mater. Mod. Process.*, 2015, **1**(5), p 1-10
40. T. Fiedler, R. Groß, J. Rösler, and M. Bäker, Damage Mechanisms of Metallic HVOF-Coatings for High Heat Flux Application, *Surf. Coat. Technol.*, 2017, **316**, p 219-225
41. R.R. Holmes, S.K. Elam, and C.A. Power, Rapid Vacuum Plasma Spray (VPS) Closeout of Liquid Rocket Engine Combustion Chamber Cooling Channels for Both Time and Cost Savings. *NASA-Report*, 2009, M09-0531
42. U. Schulz, M. Peters, F.W. Bach, and G. Tegeder, Graded Coatings for Thermal, Wear and Corrosion Barriers, *Mat. Sci. Eng. A*, 2003, **362**, p 61-80
43. S. Deshpande, S. Sampath, and H. Zhang, Mechanisms of Oxidation and Its Role in Microstructural Evolution of Metallic Thermal Spray Coatings—Case Study for Ni-Al, *Surf. Coat. Technol.*, 2006, **200**, p 5395-5406
44. S. Bose, *High Temperature Coatings*, Elsevier, Amsterdam, 2007
45. M.J. Donachie and S.J. Donachie, *Superalloys*, ASM International, Russell Township, 2002
46. P.N. Quedsted, R.F. Brooks, L. Chapman, R. Morelli, Y. Youssef, and K.C. Mills, Measurement and Estimation of Thermophysical Properties of Nickel Based Superalloys, *Mater. Sci. Technol.*, 2009, **25**, p 154-162
47. F. Traeger, R. Vaßen, K.H. Rauwald, and D. Stöver, Thermal Cycling Setup for Testing Thermal Barrier Coatings, *Adv. Eng. Mater.*, 2003, **5**(6), p 429-432
48. D. Nies, R. Pulz, S. Glaubitz, M. Finn, B. Rehmer, and B. Skrotzki, Testing of Thermal Barrier Coatings by Laser Excitation, *Adv. Eng. Mater.*, 2010, **12**, p 1224-1229
49. A. Gernoth, J. Riccius, E. Suslova, C. Böhm, E. Zametaev, L. Brummer, O.J. Haidn, B. Mewes, and K. Quering, Laser-Heating for Thermo-Mechanical Fatigue Simulation. in *IAA-RACT*, 2008
50. A. Gernoth, J.R. Riccius, and S. Schlechtriem, Optical Heating, Thermography and Deformation Measurement of Nozzle Wall Structures, in *49th AIAA Aerospace Sciences Meeting including the New Horizons Forum and Aerospace Exposition*, 2011
51. U. Rettig, U. Bast, D. Steiner, and M. Oechsner, Characterization of Fatigue Mechanisms of Thermal Barrier Coatings by a Novel Laser-Based Test, *J. Eng. Gas Turbines Power*, 1999, **121**, p 259-264
52. B.D. Choules, K. Kokini, and T.A. Taylor, Thermal Fracture of Thermal Barrier Coatings in a High Heat Flux Environment, *Surf. Coat. Technol.*, 1998, **106**, p 23-29
53. R.S. Lima and B.R. Marple, Insights on the High-Temperature Operational Limits of ZrO₂-Y₂O₃ TBCs Manufactured Via Air Plasma Spray, *J. Mater. Eng. Perform.*, 2017, **26**(3), p 1272-1282
54. R.S. Lima, B.R. Marple, and P. Marcoux, Thermal Gradient Behavior of TBCs Subjected to a Laser Gradient Test Rig: Simulation an Air-to-Air Combat Flight, *J. Therm. Spray Technol.*, 2016, **25**(1-2), p 282-290
55. M.P. Celano, H. Rochlitz, F. Hötte, O.J. Haidn, P. Scholz, and M.C. Haupt, Experimental Investigation on Heat Transfer of Rocket Combustion Chambers and Cooling Channels. in *Sonderforschungsbereich/Transregio 40—Annual Report*, 2015
56. K.P. van Hooser and D.P. Bradley, Space Shuttle Main Engine—The Relentless Pursuit of Improvement, in *AIAA SPACE 2011 Conference*, 2011
57. W. Ley, K. Wittmann, and W. Hallmann, *Handbook of Space Technology*, Wiley, Hoboken, 2009
58. K.T.K. Chiang, J.H. Arps, and R. Wei, Nanostructured Low-Cr Cu-Cr Coatings for High Temperature Oxidation Resistance. *US-Patent*, 2009, 7592051
59. M. Popp and G. Schmidt, Rocket Engine Combustion Chamber Design Concepts for Enhanced Life, in *AIAA, ASME, SAE and ASEE Joint Propulsion Conference and Exhibit No. 32*, 1996
60. R.J. Quentmeyer, Experimental Fatigue Life Investigation of Cylindrical Thrust Chambers, in *AIAA/SAE Propulsion Conference No. 13*, 1977
61. T. Fiedler, M. Bäker, and J. Rösler, Large Heat Flux Exposure of Metallic Coatings for Rocket Engine Applications, *Surf. Coat. Technol.*, 2017, **332**, p 30-39
62. Abaqus Analysis User's Manual (6.12), Dassault Systèmes, 2012
63. Kupferdatenblatt CuCr1Zr., Deutsches Kupferinstitut, 2005 (in German)
64. G. Pintsuk, J. Blumm, W. Hohenauer, R.C. Hula, T. Koppitz, S. Lindig, D. Pitzer, M. Rohde, P. Schoderböck, T. Schubert, F. Tietz, and O. Wouters, Interlaboratory Test on Thermophysical Properties of the Iter Grade Heat Sink Material Copper-Chromium-Zirconium, *Int. J. Thermophys.*, 2010, **31**, p 2147-2158
65. M. Fassin, D. Kowollik, S. Reese, K. Lindhorst, and M. Haupt, Parameter Identification and Acceleration of Fluid Structure Interaction Based Lifetime Prediction for Rocket Engine Nozzle Structures, in *Sonderforschungsbereich Transregio 40 Annual Report*, 2015
66. M. Fassin, Poissons Ratio of CuCr1Zr, Institute of Applied Mechanics RWTH Aachen University, private communication, 2015
67. Y.S. Touloukian, R.K. Kirby, R.E. Taylor, and P.D. Desai, *Thermophysical Properties of Matter 12: Thermal Expansion—Metallic Elements and Alloys*, IFI/Plenum, New York, 1975
68. K. Dies, *Kupfer und Kupferlegierungen in der Technik*, Springer, Berlin, 1967 (in German))
69. Y.S. Touloukian and E.H. Buyco, *Thermophysical Properties of Matter 4: Specific Heat—Metallic Elements and Alloys*, IFI/Plenum, New York, 1970
70. J. Wisniewski, J.M. Drezet, D. Ayrault, and B. Cauwe, Determination of the Thermophysical Properties of a CuCr1Zr Alloy from Liquid State Down to Room Temperature, *Int. J. Mater. Form.*, 2008, **1**(1), p 1059-1062
71. D. Kowollik, V. Tini, S. Reese, and M. Haupt, 3D Fluid-Structure Interaction Analysis of a Typical Liquid Rocket Engine Cycle Based on a Novel Viscoplastic Damage Model, *Int. J. Numer. Method Eng.*, 2013, **94**(13), p 1165-1190
72. R. Bürgel, H.J. Maier, and T. Niendorf, *Handbuch Hochtemperatur-Werkstofftechnik*, Vieweg, Wiesbaden, 2011 ((in German))
73. T. Fiedler, H.-R. Sinning, J. Rösler, and M. Bäker, Temperature Dependent Mechanical Properties of Metallic HVOF Coatings, *Surf. Coat. Technol.*, 2018, **349**, p 32-36
74. H.-D. Baehr and K. Stephan, *Wärme- und Stoffübertragung*, Springer, Berlin, 2016 ((in German))
75. A. Magnier, T. Wu, and T. Fiedler, Measurement of Residual Stresses in Thermal Barrier Coatings, to be published, 2019
76. A.G. Evans and W. Hutchinson, The Mechanics of Coating Delamination in Thermal Gradients, *Surf. Coat. Technol.*, 2007, **201**, p 7905-7916

77. I. Hofinger, H.A. Bahr, H. Bahlke, G. Kirchhoff, C. Häuseler, and H.J. Weiss, Fracture Mechanical Modelling and Damage Characterization of Functionally Graded Thermal Barrier Coatings by Means of Laser Irradiation, *Mater. Sci. Forum*, 1999, **308-311**, p 450-458
78. T. Fiedler, H.-R. Sinning, J. Rösler, and M. Bäker, Material Parameter Identification for Finite Element Modelling of Coatings for Rocket Combustion Chambers, in *Sonderforschungsbereich/Transregio 40—Annual Report 2017*, 2017
79. J.W. Hutchinson, M.Y. He, and A.G. Evans, The Influence of Imperfections on the Nucleation and Propagation of Buckling Driven Delaminations, *J. Mech. Phys. Solids*, 2000, **48**, p 709-734
80. A.G. Evans, D.R. Mumm, J.W. Hutchinson, G.H. Meier, and F.S. Pettit, Mechanisms Controlling the Durability of Thermal Barrier Coatings, *Prog. Mater. Sci.*, 2001, **46**, p 505-553
81. J.W. Hutchinson, Stress and Failure Modes in Thin Films and Multilayers. Technical University of Denmark, Notes for a DCAMM Course, 1996
82. J.W. Hutchinson, M.D. Thouless, and E.G. Liniger, Growth and Configurational Stability of Circular Buckling-Driven Film Delaminations, *Acta Metall. Mater.*, 1992, **40(2)**, p 295-308
83. S.P. Timoshenko and J.M. Gere, *Theory of Elastic Stability*, McGraw-Hill International Book Company, New York City, 1985
84. M. Bäker, Finite Element Simulation of Interface Cracks in Thermal Barrier Coatings, *Comput. Mater. Sci.*, 2012, **64**, p 79-83
85. A.G. Evans, M.Y. He, and J.W. Hutchinson, Effect of Interface Undulations on the Thermal Fatigue of Thin Films and Scales on Metal Substrates, *Acta Mater.*, 1997, **45(9)**, p 3543-3554
86. M. Bäker and P. Seiler, A Guide to Finite Element Simulations of Thermal Barrier Coatings, *J. Therm. Spray Technol.*, 2017, **26(6)**, p 1146-1160

Publisher's Note Springer Nature remains neutral with regard to jurisdictional claims in published maps and institutional affiliations.